IMPROVING JOINT LEARNING OF SUSPENDED AND ADHERENT CELL DETECTION USING LOW-PASS MONOGENIC PHASE AND TRANSPORT OF INTENSITY EQUATION

F. Mualla[1], *S. Schöll*[1,2,3], *B. Sommerfeldt*[4], *S. Steidl*[1], *R. Buchholz*[4], *J. Hornegger*[1,3]

[1]Pattern Recognition Lab, Friedrich-Alexander University, Erlangen, Germany
[2]ASTRUM IT GmbH, Erlangen, Germany
[3]SAOT Graduate School in Advanced Optical Technologies, Erlangen, Germany
[4]Institute of Bioprocess Engineering, Friedrich-Alexander University, Erlangen, Germany

ABSTRACT

Defocusing is used in bright-field image processing in order to increase image contrast. Moreover, defocused images can be used to solve the transport of intensity equation (TIE) and obtain physical light phase. Recently, it was shown that the monogenic local features of an axial intensity derivative passed through a specific low-pass filter can be used to improve cell segmentation. In this paper, we show that the TIE solution and the low-pass monogenic local phase (LMLP) can be successfully employed for improving joint learning of adherent and suspended cell detection. A state-of-the-art approach for cell detection on defocused images reported 10.4% decrease in F-measure of suspended cell detection when trained on both adherent and suspended cell lines compared to the case when training was done for each cell line separately. Using TIE solution for feature extraction instead of a defocused image, joint training was drastically improved and the aforementioned difference in F-measure was reduced to 2%. LMLP, achieved approximately the same result, though a bit inferior.

1. INTRODUCTION

The problem of cell detection in microscope images was addressed by several research papers in the last few years [1–9]. The difficulty of the problem is inherently related to image modality. Bright-field microscopy exhibits much lower contrast compared to phase-contrast and fluorescence microscopy [10, 11]. It is possible to gain more contrast by defocusing the microscope [12]. In fact, the axial intensity derivative, i.e. the derivative of image intensity with respect to the defocus distance, is related to light phase through the transport of intensity equation (TIE) [13].

In [7] and [9], defocused images were directly used for image processing and/or feature extraction. On the other hand, in [10], the defocused images were used for solving the TIE and obtaining a quantitative phase map. Segmentation was then applied on the reconstructed phase image. Rather than directly solving the TIE, in [14], the local phase, local orientation, and local energy of light phase were approximated using a low-pass monogenic signal framework. The aforementioned local phase and orientation were used in [15] for adherent cell segmentation, while it was shown in [16] that the local phase is better than a defocused image for pixel-patch cell/background classification.

Recently, [7] obtained high detection accuracy on defocused bright-field images. However, the detection error when the algorithm was trained using both suspended and adherent cell lines was higher compared to the case when the algorithm was trained separately for each cell line. This is probably due to differences in contrast and cellular details between adherent and suspended cells (cf. Figure 1). In this paper, we show that it is possible to considerably improve the joint training of adherent and suspended cell lines, if a TIE solution image or local phase of the low-pass monogenic signal framework are used for feature extraction instead of a defocused image.

The evaluation was done on two adherent cell lines and one suspended cell line. The adherence state applies to the vast majority of cells in the adherent cell lines. However, there were also some cells in suspension because it was not possible to force all cells to adhere during the cultivation process. In fact, suspended and adherent cells coexist in cell cultures in the general case. Therefore, improving joint learning has a real practical importance.

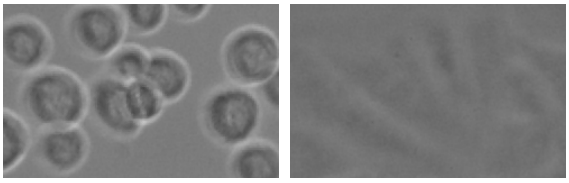

(a) Suspended Sf21 cells at defocus distance 15 μm (b) Adherent CHO cells at defocus distance 30 μm

Fig. 1: Differences in visual appearance between suspended and adherent cells. Defocus distances were experimentally chosen to maximize contrast. Original contrast was kept in order to show the difference in dynamic range.

2. MATERIALS AND METHODS

2.1. Transport of intensity equation

A relation between the physical phase of light φ and the axial intensity derivative $\frac{\partial I}{\partial z}$ was derived by Teague [13]:

$$-\frac{2\pi}{\lambda}\frac{\partial I}{\partial z} = \nabla \cdot (I \nabla \varphi) \tag{1}$$

where λ is the wavelength of light, z is the axial distance to the focus position, and I is the intensity image at focus. The gradient ∇ and the divergence $\nabla\cdot$ operators are defined in the lateral plane, i.e the 2D image plane. Eq. (1) can be solved analytically for φ [17]:

$$\varphi = -\frac{2\pi}{\lambda}\nabla^{-2}\left(\nabla\cdot\left(\frac{1}{I}\nabla\nabla^{-2}\frac{\partial I}{\partial z}\right)\right) \tag{2}$$

where ∇^{-2} is the inverse Laplacian operator.

2.2. Low-pass monogenic local phase

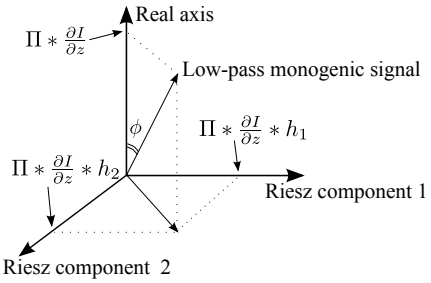

Fig. 2: An illustration of the low-pass monogenic local phase represented by the angle ϕ.

The monogenic signal [18] of a 2D image $S(x, y)$ can be defined as a quaternion-valued function of the spatial coordinates x and y whose real part is the signal S itself while its vector part is the Riesz transform of the signal. Riesz transform is a vector-valued function with two components, and hence the quaternion in this case is 3-dimensional. Monogenic local phase is then defined in terms of the angle between the 3D quaternion vector and the quaternion's real part axis. Typically, a band-passed version of the considered signal is used to compute local phase. In [14], it was suggested to approximate TIE solution in the monogenic domain by computing the monogenic representation of a low-passed version of an axial derivative image instead of the typically used band-passed version of the image. According to this suggestion, the low-pass monogenic local phase (LMLP) is given by the following equation:

$$\phi = \arctan\frac{\sqrt{(\Pi * \frac{\partial I}{\partial z} * h_1)^2 + (\Pi * \frac{\partial I}{\partial z} * h_2)^2}}{\Pi * \frac{\partial I}{\partial z}} \tag{3}$$

where h_1 and h_2 are the two Riesz transform kernels. Π is a low-pass filter which resembles the inverse Laplacian. The reader is referred to [19] for the definitions of Riesz kernels and to [14] for details about Π. An illustration of the LMLP and Eq. (3) can be seen in Figure 2.

In fact, Eq. (3) computes the monogenic local phase of $\Pi * \frac{\partial I}{\partial z}$. The connection to TIE becomes clear in the special case when I can be considered uniform in the lateral plane. Under this condition, a simpler expression for φ than Eq. (2) can be directly derived from Eq. (1):

$$\hat{\varphi} = c\nabla^{-2}\left(\frac{\partial I}{\partial z}\right) \tag{4}$$

where c is a constant related to wavelength and the uniform intensity value. Therefore, Eq. 3 computes the local phase of an approximation of physical light phase.

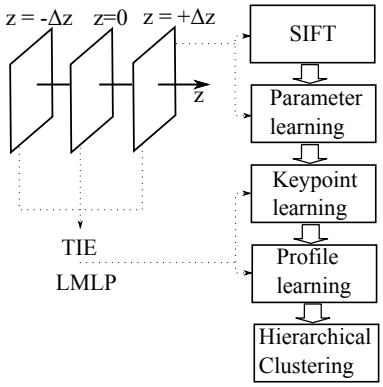

Fig. 3: The proposed cell detection pipeline

2.3. Cell detection pipeline

We use the automatic detection pipeline of [7]: SIFT keypoints [20] are extracted from a defocused image. These keypoints are classified using a random forest into background or cell keypoints. Background keypoints are discarded while a profile is extracted between each two nearby cell keypoints and classified using another random forest into either a *cross* or *inner* profile. A profile is *inner* if the two corresponding keypoints belong to the same cell, otherwise it is *cross*. The probabilistic output of the profile classifier is used as input for a hierarchical clustering step with a customized linkage method. A weighted average of the keypoint coordinates in each cluster represents a detected cell center. The keypoint features, the profile features, and the system parameters are highly invariant to scale, orientation, and illumination conditions.

In contrast to [7], we extract the keypoint features and the profile features from a TIE solution image or an LMLP image instead of a defocused image. However, similar to [7], we use the defocused image for keypoint extraction and parameter learning. Figure 3 clarifies the structure of the proposed pipeline.

The difference of two defocused images at distances $\pm\Delta z$ is used as an estimation of the axial derivative. LMLP is then computed directly using Eq. (3). The exact values of Δz for each cell line are given in Section 2.4. The estimated axial derivative and the image at-focus are used to compute the TIE solution using Eq. (2). The inverse Laplacian in Eq. (2) is performed by applying a Fourier-based method [21]. Usually, the resulting solution is contaminated with a low-frequency bias field. The latter is estimated using a thin-plate smoothing spline approach and subtracted from the TIE solution.

2.4. Materials

As described in Table 1, we use three cell lines containing together 16 image sets[1]. Each image set is composed of a negatively defocused image at defocus distance $-\Delta z$ (Figure 4a), an image at focus (Figure 4b), and a positively defocused image at defocus distance $+\Delta z$ (Figure 4c). These images were acquired with an inverted Nikon Eclipse TE2000U microscope and Nikon's USB camera using a 20x objective. The used Δz values are listed in Table 1. The software package SePhaCe [15] was used to generate an LMLP image (Figure 4d) and a TIE solution image for each image set. SePhaCe

[1]Available online with their corresponding ground-truth masks (cell-boundary delineation) at `http://www5.cs.fau.de/~mualla/#imagedb`

was also used for the bias correction step (cf. Section 2.3). A thin-plate smoothing spline was estimated for each TIE solution image (1280 x 960 pixels) over a grid of 50 x 50 points. Figure 4e exemplifies the TIE solution after the bias-field subtraction.

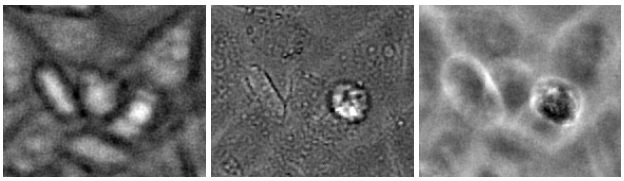

(a) Negatively defocused (b) At focus (c) Positively defocused

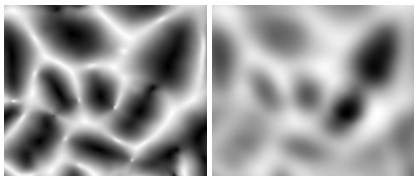

(d) LMLP (e) TIE solution after bias correction

Fig. 4: Patches extracted from an L929 image set. The histogram of each patch was linearly stretched in the range $[0, 255]$ for clarity.

Table 1: Summary of the cell lines used in the evaluation

Cell line	State	Image sets	Cells	Δz (μm)
CHO	Adherent	6	1431	30
L929	Adherent	5	1078	30
Sf21	Suspended	5	1001	15

3. EVALUATION

In order to evaluate [7] for joint learning of Sf21 and L929, a positively defocused image of each of the two cell lines was randomly chosen. The two images were used to train the system. The trained system was then tested on the rest of the positively defocused images in L929 and Sf21 and a mean F-measure value was obtained. This process was repeated five times with a mean F-measure value obtained from each repetition. The average and the standard deviation of these five mean F-measure values can be seen at the left-hand side of the first row of Table 2. Since adherent and suspended cell images have different dynamic ranges, each image was normalized to $[0, 1]$ before being used for training or testing.

The right-hand side of the first row shows F-measure results for separate training. In this case, one image is used for training in each cell line and tested on the other images of the same cell line. This is repeated in a cross-validation loop.

We evaluated our approach for joint and separate training in the same manner as described above. However, as explained in Section 2.3, LMLP and TIE solution images are used for feature extraction. The second row of Table 2 shows the F-measure results when TIE solution is used for keypoint and profile feature extraction. The third row shows the results when LMLP images are used for feature extraction. And lastly, the fourth row is dedicated to the case when TIE solution is used for keypoint feature extraction while LMLP is used for profile feature extraction.

In Table 3, the same experiment was performed but with CHO as adherent cell line instead of L929. It is possible to average the results obtained from Table 2 and Table 3 and shape the figures in terms of suspended and adherent cell lines. This can be seen in Table 4. In this table, one can notice that the F-measure on suspended cells using [7] was reduced from 97.0 in separate training to 86.6 in joint training. When, for instance, TIE solution was employed for keypoint and profile feature extraction, F-measure on suspended cells was recovered to 95.7 while F-measure on adherent cells degraded with a very small amount (from 84.2 to 83.6). In order to draw conclusions more easily, in Table 5 we aggregate the results of Table 4 in terms of total loss in F-measure, i.e. the loss in F-measure on adherent cells added to the F-measure loss on suspended cells. One can see that the minimum loss in joint training is obtained when TIE solution is used for keypoint feature extraction and LMLP is used for profile feature extraction. The other two cases (TIE alone or LMLP alone) were a bit inferior to TIE with LMLP, but very close to it. On the other hand, in separate training, the difference between all four cases was small. Nevertheless, our approach achieved a bit higher separate-learning F-measure compared to [7].

Table 2: F-measure values of our approach and [7] for L929 and Sf21. K denotes the image used for keypoint feature extraction while P denotes the image used for profile feature extraction.

	Joint learning		Separate learning	
	L929	Sf21	L929	Sf21
Mualla et al. [7]	85.3±2.1	86.7±2.4	86.5±1.3	97.0±1.2
K=TIE P=TIE	84.5±2.1	95.7±0.4	87.1±1.7	97.7±0.9
K=LMLP P=LMLP	83.6±1.9	95.5±1.5	85.7±1.9	98.2±0.7
K=TIE P=LMLP	84.2±2.2	96.5±0.6	86.9±1.7	97.8±0.9

Table 3: F-measure values of our approach and [7] for CHO and Sf21. K denotes the image used for keypoint feature extraction while P denotes the image used for profile feature extraction.

	Joint learning		Separate learning	
	CHO	Sf21	CHO	Sf21
Mualla et al. [7]	83.1±4.0	86.5±3.3	84.2±3.4	97.0±1.2
K=TIE P=TIE	82.7±3.4	95.7±1.4	84.4±2.5	97.7±0.9
K=LMLP P=LMLP	81.6±2.7	94.5±1.8	83.9±2.3	98.2±0.7
K=TIE P=LMLP	83.0±3.6	96.1±1.1	84.1±2.5	97.8±0.9

4. DISCUSSION

We showed that LMLP and TIE solution yield considerably better joint learning of adherent and suspended cell detection. Our dataset does not contain focus stacks. Therefore, no evaluation of the effect of the defocus distance choice Δz was performed. In [16], the same dataset was used for assessing the discriminative power of LMLP in patch-wise cell/background classification. As stated in [16], by defocusing the microscope, two effects work together: the blurring by the point spread function of the objective and the increased contrast modeled by TIE. Therefore, there is a value which maximizes the obtained contrast by avoiding excessive smoothing with large distances

Table 4: F-measure values of our approach and [7] averaged from Table 2 and Table 3. K denotes the image used for keypoint feature extraction while P denotes the image used for profile feature extraction.

	Joint learning		Separate learning	
	Adherent	Suspended	Adherent	Suspended
Mualla et al. [7]	84.2	86.6	85.3	97.0
K=TIE P=TIE	83.6	95.7	85.7	97.7
K=LMLP P=LMLP	82.6	95.0	84.8	98.2
K=TIE P=LMLP	83.6	96.3	85.5	97.8

Table 5: Total F-measure loss of our approach and [7]. K denotes the image used for keypoint feature extraction while P denotes the image used for profile feature extraction.

	Joint learning	Separate learning
Mualla et al. [7]	29.2	17.6
K=TIE P=TIE	20.7	16.5
K=LMLP P=LMLP	22.4	17.0
K=TIE P=LMLP	20.1	16.7

and avoiding noise dominance and insufficient contrast with small distances. This optimum was experimentally chosen in our dataset. In other words, the defocus distance was chosen based on a contrast-blurring trade-off. Compared to published phase retrieval results for cell segmentation [10, 15], our phase images look blurred. Therefore, shorter distances are needed for border delineation. However, our concern is to maximize contrast for cell detection applications rather than cell segmentation. Consequently, using the aforementioned contrast-blurring trade-off principle for the defocus distance selection sounds plausible. An ongoing research in our group is currently conducted to choose the defocus distance automatically based on this principle.

ACKNOWLEDGMENT

The authors would like to thank the Bavarian Research Foundation BFS for funding the project COSIR under contract number AZ-917-10. In addition, we gratefully acknowledge funding of the Erlangen Graduate School in Advanced Optical Technologies (SAOT) by the German Research Foundation (DFG) in the framework of the German excellence initiative.

5. REFERENCES

[1] T.W. Nattkemper, H. Ritter, and W. Schubert, "Extracting patterns of lymphocyte fluorescence from digital microscope images," *Intelligent Data Analysis in Medicine and Pharmacology*, vol. 99, pp. 79–88, 1999.

[2] X. Long, W.L. Cleveland, and Y.L. Yao, "A new preprocessing approach for cell recognition," *IEEE Transactions on Information Technology in Biomedicine*, vol. 9, no. 3, pp. 407–412, 2005.

[3] X. Long, W.L. Cleveland, and Y.L. Yao, "Automatic detection of unstained viable cells in bright field images using a support vector machine with an improved training procedure," *Computers in Biology and Medicine*, vol. 36, no. 4, pp. 339–362, 2006.

[4] Zhaozheng Yin, R. Bise, Mei Chen, and T. Kanade, "Cell segmentation in microscopy imagery using a bag of local bayesian classifiers," in *Biomedical Imaging: From Nano to Macro, 2010 IEEE International Symposium on*, 2010, pp. 125–128.

[5] C. Arteta, V. Lempitsky, J. A. Noble, and A. Zisserman, "Learning to detect cells using non-overlapping extremal regions," in *International Conference on Medical Image Computing and Computer Assisted Intervention*, N. Ayache, Ed. MICCAI, 2012, Lecture Notes in Computer Science, pp. 348–356, Springer.

[6] J. Pan, T. Kanade, and M. Chen, "Learning to detect different types of cells under phase contrast microscopy," in *Microscopic Image Analysis with Applications in Biology*, September 2009.

[7] F. Mualla, S. Schöll, B. Sommerfeldt, A. Maier, and J. Hornegger, "Automatic cell detection in bright-field microscope images using SIFT, random forests, and hierarchical clustering," *Medical Imaging, IEEE Transactions on*, vol. 32, no. 12, pp. 2274–2286, December 2013.

[8] Jiyan Pan, Takeo Kanade, and Mei Chen, "Heterogeneous conditional random field: Realizing joint detection and segmentation of cell regions in microscopic images," in *Computer Vision and Pattern Recognition (CVPR), 2010 IEEE Conference on*, 2010, pp. 2940–2947.

[9] G. Becattini, L.S. Mattos, and D.G. Caldwell, "A novel framework for automated targeting of unstained living cells in bright field microscopy," in *Proceedings of the IEEE International Symposium on Biomedical Imaging: From Nano to Macro*, April 2011, pp. 195–198.

[10] C.L. Curl, T. Harris, P.J. Harris, B.E. Allman, C.J. Bellair, A.G. Stewart, and L.M.D. Delbridge, "Quantitative phase microscopy: a new tool for measurement of cell culture growth and confluency in situ," *Pflügers Archiv European Journal of Physiology*, vol. 448, no. 4, pp. 462–468, 2004.

[11] M. Tscherepanow, F. Zöllner, M. Hillebrand, and F. Kummert, "Automatic segmentation of unstained living cells in bright-field microscope images," in *Advances in Mass Data Analysis of Images and Signals in Medicine, Biotechnology, Chemistry and Food Industry*, vol. 5108 of *Lecture Notes in Computer Science*, pp. 158–172. Springer, 2008.

[12] U. Agero, C. H. Monken, C. Ropert, R. T. Gazzinelli, and O. N. Mesquita, "Cell surface fluctuations studied with defocusing microscopy," *Physical Review E*, vol. 67, no. 5, pp. 051904, 2003.

[13] Michael Reed Teague, "Deterministic phase retrieval: a green's function solution," *Journal of the Optical Society of America*, vol. 73, no. 11, pp. 1434–1441, 1983.

[14] R. Ali, T. Szilagyi, M. Gooding, M. Christlieb, and M. Brady, "On the use of low-pass filters for image processing with inverse laplacian models," *Journal of Mathematical Imaging and Vision*, pp. 1–10, 2010.

[15] R. Ali, M. Gooding, T. Szilágyi, B. Vojnovic, M. Christlieb, and M. Brady, "Automatic segmentation of adherent biological cell boundaries and nuclei from brightfield microscopy images," *Machine Vision and Applications*, vol. 23, no. 4, pp. 607–621, 2012.

[16] Firas Mualla, Simon Schöll, Björn Sommerfeldt, and Joachim Hornegger, "Using the Monogenic Signal for Cell-Background Classification in Bright-Field Microscope Images," in *Proceedings des Workshops Bildverarbeitung für die Medizin 2013*, 2013, pp. 170–174.

[17] David Paganin and Keith A Nugent, "Noninterferometric phase imaging with partially coherent light," *Physical review letters*, vol. 80, no. 12, pp. 2586–2589, 1998.

[18] M. Felsberg and G. Sommer, "The monogenic signal," *IEEE Transactions on Signal Processing*, vol. 49, no. 12, pp. 3136–3144, 2001.

[19] Elias M Stein, *Singular integrals and differentiability properties of functions Elias M. Stein.*, vol. 2, Princeton university press, 1970.

[20] D.G. Lowe, "Distinctive image features from scale-invariant keypoints," *International Journal of Computer Vision*, vol. 60, no. 2, pp. 91–110, November 2004.

[21] VV Volkov, Y Zhu, and M De Graef, "A new symmetrized solution for phase retrieval using the transport of intensity equation," *Micron*, vol. 33, no. 5, pp. 411–416, 2002.